Scaling functions in the soft-wall AdS/QCD models

Zhongzheng Zhang,[1] Danning Li,[1,*] Lang Yu,[2,†] Zhibin Li,[3] and Xinyang Wang[4]
[1]*Department of Physics and Siyuan Laboratory, Jinan University, Guangzhou 510632, China*
[2]*College of Physics, Jilin University, Changchun 130012, People's Republic of China*
[3]*Institute for Astrophysics, School of Physics, Zhengzhou University, Zhengzhou 450001, China*
[4]*Fundamental Physics Center, School of Mechanics and Physics, Anhui University of Science and Technology, Huainan, Anhui 232001, China*

(Received 6 August 2025; accepted 27 March 2026; published 28 April 2026)

We investigate the static scaling behavior of the chiral condensate near the two-flavor critical point within the framework of the soft-wall AdS/QCD. The scaling functions are extracted from the chiral order parameters and are found to precisely match those obtained through mean-field calculations. Additionally, it is also checked that the scaling functions are independent of the specific construction of the holographic model. Furthermore, we develop the formalism for calculating the chiral susceptibility and demonstrate that the pseudocritical temperatures obey the scaling law for moderate quark masses. It is shown that the temperature scaling could be comparable with those obtained from Dyson-Schwinger equations and lattice simulations. While the soft-wall AdS/QCD framework predicts mean-field critical exponents that are universal, the critical coefficients and the crossover dynamics are model dependent and provide quantitative constraints for phenomenological model building. These findings could help improve the effectiveness of the soft-wall AdS/QCD.

DOI: 10.1103/7njb-6v24

I. INTRODUCTION

Empirical and lattice-QCD studies indicate that, at nonzero temperature and baryon chemical potential, QCD undergoes two intertwined but conceptually distinct phase transitions: deconfinement, whereby color degrees of freedom become manifest over hadronic scales, and chiral-symmetry restoration characterized by the melting of the quark condensate. Clarifying the interplay between these two phenomena is essential for interpreting experimental observables in heavy-ion collisions, elucidating the equation of state of dense matter in compact stars and constraining scenarios for the evolution of the early Universe [1–4].

For physical quark masses, lattice-QCD studies establish that QCD matter undergoes a smooth analytic crossover at vanishing baryon chemical potential [5–8]. In the two-flavor chiral limit, by contrast, the transition becomes a true phase transition whose order—second or first—depends on the relative hierarchy between chiral-symmetry restoration and the effective restoration of the axial $U(1)$ anomaly [5]. Besides its theoretical significance, mapping the QCD phase diagram in the quark-mass plane is essential for locating the critical end point (CEP), a primary objective of present heavy-ion-collision experiments; in particular, the chiral-limit transition temperature provides an upper bound for possible CEP temperatures at nonzero baryon chemical potential [9]. Since lattice simulations cannot be carried out directly in the exact chiral limit, analyses that exploit universal scaling functions are indispensable for extrapolating physical results to that limit.

Recent lattice-QCD results have revealed the anticipated $O(N)$ scaling behavior [10–12] of the chiral crossover. The connection based on the universal scaling equation is restricted to a finite domain referred to as the scaling window. The width of this window is still under debate. According to lattice-QCD results [13,14], the scaling region is located at relatively large values of the pion mass. Reference [15], for example, explores the conformal window across different flavor numbers and suggests that, within the 3D $O(4)$ universality class, the physical pion mass may lie close to the critical point, with scaling behavior potentially extending into the high-temperature regime up to 300 MeV. In contrast, another lattice-QCD study [16] indicates that the scaling window may also extend below the physical quark mass and, based on the scaling function, provides an estimate of the transition temperature in the chiral limit. Consistently, alternative approaches such as Dyson-Schwinger equations (DSEs) [9,17,18] and the functional renormalization group (FRG) [19,20] also

*Contact author: lidanning@jnu.edu.cn
†Contact author: yulang@jlu.edu.cn

demonstrate the presence of scaling behavior for quark masses below the physical point.

In the low-energy regime where QCD phase transitions take place, the strong coupling strength renders conventional perturbative techniques inadequate. Thus, it is essential to develop nonperturbative methods to explore the underlying physics. Among such methods, lattice QCD—formulated from first principles—has been recognized as a reliable tool. However, at large baryon densities, lattice QCD suffers from the notorious sign problem [21], which has yet to be satisfactorily resolved. This limitation has motivated the search for alternative nonperturbative approaches.

In the 1990s, 't Hooft proposed a preliminary form of the holographic principle [22], which was subsequently integrated with string theory by Susskind [23]. The AdS/CFT correspondence, first conjectured by Maldacena [24], has shed new light on solving strongly coupled problems in gauge field theories. In the study of QCD matter, a celebrated achievement of holographic approaches is the derivation of the universal lower bound $\eta/s = 1/(4\pi)$ for the shear viscosity to entropy density ratio, providing key insight into the nearly perfect-fluid behavior of the quark-gluon plasma from a theoretical perspective [25–27]. Employing a bottom-up strategy that prioritizes phenomenology over top-down string-theoretic origins, researchers have constructed a variety of holographic models—including light-front holographic QCD [28], holographic model of QCD in the Veneziano limit [29], and Einstein–Maxwell–Dilaton (EMD) setups [30–36]—to capture hadron spectra, thermodynamics, transport coefficients, and the QCD phase transition with remarkable success. From those phenomenological studies, it appears that the EMD model provides an adequate description of gluodynamics.

It has been shown that spontaneous chiral-symmetry breaking, as another key low-energy feature of QCD, can be effectively described within the hard-wall and soft-wall AdS/QCD models [37,38]. A finite chiral condensate is dynamically generated, lifting the degeneracy between chiral partners in the hadron spectrum [39,40]. As the temperature increases, this condensate is progressively suppressed; once it vanishes, chiral symmetry is restored and the chiral phase transition takes place [41,42].

The principal advantage of this model is that by elevating the four-dimensional (4D) global symmetry to a five-dimensional (5D) gauge symmetry, it naturally incorporates the conserved currents and the $\bar{q}q$ bilinear operator. This makes it straightforward to explore scenarios with arbitrary quark masses and finite charge densities. Studies have extended from simple two-flavor systems to $N_f = 2 + 1$ [43–45], and more recently to $N_f = 2 + 1 + 1$ [46]. The phase diagram in the quark-mass plane $(m_{u/d} - m_s)$ can be summarized in a holographic version [47] of the so-called "Columbia plot," which qualitatively agrees well with that obtained by combining the lattice simulations and other effective studies [8,48]. By introducing the baryon and isospin chemical potentials μ_B and μ_I through the corresponding conserved currents, one can probe regimes of high baryon and isospin densities where recent studies predict the appearance of additional phases, e.g., the quarkyonic and pion-condensed phases [49–52]. A magnetic field can be introduced by constructing the electromagnetic current from the baryon and isospin currents; inverse magnetic catalysis then emerges naturally, without fine-tuning of the model settings [53,54]. Furthermore, as derived in [55], the model can be reduced to a four-dimensional chiral perturbation theory. The matching of the near T_c behavior of its Goldstone modes [56–58] with those of the four-dimensional chiral perturbation theory [59] provides explicit evidence for this equivalence. Overall, the soft-wall model offers an excellent starting point for exploring chiral dynamics in QCD, serving in effect as a five-dimensional analog of chiral perturbation theory.

Although the above analyses have thoroughly validated the soft-wall model's consistency and effectiveness in describing low-energy QCD, its universality has yet to be fully tested. While the critical exponents have been proved to be of mean-field level [47], with $\beta = 1/2$, $\delta = 3$ in the two-flavor limit, the holographic investigation of mass scaling behavior of the pseudocritical temperature, as well as of the scaling function itself, remains largely undeveloped. Given that universal scaling functions enable chiral extrapolation in lattice QCD and are important for constraining holographic model building (while fitting at the physical point is valuable, it alone cannot fully validate a holographic model's robustness), in this work, we aim to investigate the scaling behavior of the chiral phase transition temperature T_c with respect to different quark and pion masses. We will calculate the scaling function and test the scaling window in the holographic model, which may provide further constraints for building a realistic holographic QCD model. In this work, we will focus on the two-flavor limit for simplicity.

The organization of this paper is as follows: In Sec. II, we briefly review the soft-wall model and chiral phase transition in this model. In Sec. III, we numerically extract the scaling functions and test the universal relations of those functions as a check of the self-consistency of the soft-wall AdS/QCD models. In Sec. IV, we give analyses of the scaling behavior of the pseudocritical temperature. An additional constraint is given for constructing a more realistic holographic QCD model for chiral dynamics. Finally, a brief summary will be given in Sec. V.

II. THE SOFT-WALL ADS/QCD MODEL

In this section, we provide a brief overview of the soft-wall model and introduce several modifications to explore its universal properties. As discussed above, the action of the soft-wall model is constructed by promoting the 4D global chiral symmetry $SU(2)_L \otimes SU(2)_R$ to 5D gauge

symmetry. Since we focus on the two-flavor limit, i.e., considering only the u and d quarks, the action of the soft-wall model is given as follows:

$$S_{5D} = \int d^5x\sqrt{g}e^{-\Phi}\mathrm{Tr}\Big\{|D_M X|^2 - V_X(|X|) - \frac{1}{4g_5^2}(F_L^2 + F_R^2)\Big\}. \tag{1}$$

In the above action, M represents spacetime indices, g is the determinant of the metric g_{MN}, X is an $N_f \times N_f$ matrix-valued scalar field, and Φ is the dilaton field. As in previous studies, we set the dilaton field as

$$\Phi = \mu_g^2 r^2, \tag{2}$$

with r being the holographic dimension. The 5D coupling constant g_5 can be determined as $g_5^2 = \frac{12\pi^2}{N_c}$ by matching the large-momentum expansion of the vector current $J_\mu^a = \bar{q}\gamma_\mu t^a q$ correlation in AdS/QCD with that from the perturbative calculation [37]. The covariant derivative D_M and the field strength tensors $F_{MN}^{L,R}$ are defined as follows:

$$\begin{aligned} D_M X &= \partial_M X - iL_M X + iXR_M, \\ F_{MN}^L &= \partial_M L_N - \partial_N L_M - i[L_M, L_N], \\ F_{MN}^R &= \partial_M R_N - \partial_N R_M - i[R_M, R_N], \end{aligned} \tag{3}$$

with L_M, R_M being the 5D left- and right-handed gauge potentials, which are dual to the left- and right-handed chiral currents. $V_X(|X|)$ represents the scalar potential, which may generally include a coupling to the dilaton field. Since we consider the degenerate two-flavor case ($m_u = m_d$) only, the expectation of X can be decomposed as $X = \frac{1}{2}\chi I_2$, with I_2 the 2×2 identity matrix. The factor $1/2$ is introduced to ensure that the kinetic term in χ is canonical. Then we denote the scalar potential in terms of χ as $V(\chi) = \mathrm{Tr}[V_X(X)]$. Since we do not consider the case with finite densities or consider the vector perturbations, the relevant part of the action reduces to

$$S_{5D} = \int d^5x\sqrt{g}e^{-\Phi}\left[\frac{1}{2}\chi'^2 - V(\chi)\right]. \tag{4}$$

To study chiral dynamics in this model, a specific form of the background metric is necessary. In consideration of the symmetries of the four-dimensional theory at finite temperature, the metric ansatz is adopted as follows:

$$ds^2 = e^{2A(r)}\left(f(r)dt^2 - dx^2 - \frac{1}{f(r)}dr^2\right). \tag{5}$$

A simple consideration is to take the AdS-Schwarzschild black hole solution with

$$\begin{aligned} A(r) &= -\ln(r), \\ f(r) &= 1 - \frac{r^4}{r_h^4}. \end{aligned} \tag{6}$$

Here, r_h denotes the black hole horizon, at which the blackening factor satisfies $f(r_h) = 0$. This can be mapped to the temperature through the Hawking temperature defined as

$$T = \left|\frac{f'(r_h)}{4\pi}\right| = \frac{1}{\pi r_h}. \tag{7}$$

To solve this model, one has to derive the equation of motion for χ from the action Eq. (4), which reads

$$\chi'' + \left(3A' + \frac{f'}{f} - \Phi'\right)\chi' - \frac{e^{2A}}{f}V_\chi(\chi) = 0, \tag{8}$$

with $V_\chi(\chi) \equiv \partial_\chi V(\chi)$. Here we have assumed that the system is in an equilibrium state, so χ depends on r only. The overprime $'$ in the above equation denotes differentiation with respect to r.

It is not difficult to derive from the above equation the near boundary ($r = 0$) and near horizon ($r = r_h$) expansion of χ as

$$\chi(r \to 0) = m_q\zeta r + \cdots + \frac{r^3\sigma}{\zeta} + \mathcal{O}(r^4), \tag{9a}$$

$$\chi(r \to r_h) = c_0 - \frac{V'(c_0)}{4r_h}(r - r_h) + \mathcal{O}(r - r_h)^2, \tag{9b}$$

where m_q and $\sigma \equiv \langle\bar{q}q\rangle$ are two independent integration constants in the UV region, dual to the quark mass and the chiral condensate, respectively. c_0 is an integration constant in the IR region and $c_0 \equiv \chi(r_h)$. In Ref. [60], ζ is identified as a normalization constant with the value $\zeta = \frac{\sqrt{N_c}}{2\pi}$, which is obtained by mapping the correlation of the scalar operator to that from the 4D perturbative calculation. Here, we will take $N_c = 3$. One of the integration constants in the IR region is discarded due to its association with a divergent solution at r_h. Thus, c_0 is kept as the only coefficient corresponding to a regular solution at the horizon.

This study focuses on the scaling behavior of the chiral phase transition temperature. By utilizing the asymptotic expansions of the solutions near the UV boundary $r = 0$ and the IR horizon $r = r_h$ as provided in Eqs. (9a) and (9b), the boundary-valued problem can be reformulated as an iterative problem following the procedure established in our previous work [42,57]. This enables the application of the "shooting method" [61] to extract the chiral condensate σ. Before one can work it out, the scalar potential should be specified as well.

TABLE I. Fitting parameters in model I.

Parameters	m_{phy} (MeV)	μ_g (MeV)	μ_c (GeV)	λ
Value	3.22	0.44	1.45	80

TABLE II. Fitting parameters in model II.

Parameters	m_{phy} (MeV)	μ_g (MeV)	γ	λ	κ
Value	3.90	0.35	6	25	0.85

Following our previous study [42], we choose the scalar potential to be

$$V(\chi) = \frac{1}{2}m_5^2(r)\chi^2 + \frac{\lambda}{8}\chi^4. \tag{10}$$

Here, one can assume a general coupling between the scalar field and the dilaton field, such as $g_2(\phi)\chi^2$ and $g_4(\phi)\chi^4$ with g_2, g_4 two coupling functions. In this case, effective r-dependent $m_5^2(r)$ and $\lambda(r)$ can be introduced. That is why we treat m_5^2 and λ as r-dependent functions in the above potential. Following Ref. [45], we will take

$$\text{Model I}: \; m_5^2(r) = -3 - \mu_c^2 r^2 \tag{11}$$

and a constant λ, which we will call "model I." Here, the leading term -3 comes from the AdS/CFT prescription $M_5^2 = (d-p)(d+p-4)$ with the dimension $d = 3$, and $p = 0$ for the scalar $\bar{q}q$ operator. Following Ref. [62], we will take

$$\text{Model II}: \; m_5^2(r) = -3[1 + \gamma \tanh(\kappa\Phi)] \tag{12}$$

and a constant λ, which we will call "model II." The light meson spectra have been carefully studied in these two models, and the model parameters are fitted as shown in Table I for model I and in Table II for model II, which are taken from Refs. [45,62], respectively. The quark mass enters the two models through the boundary expansion of χ, and the physical values m_{phy} in Tables I and II give pion masses around the experimental value (we take 139.6 MeV). Here, the pion masses can be obtained by considering the perturbation of the Goldstone modes (for details, please refer to Refs. [37,38]).

Inserting the parameters in Tables I and II and into the two models, one can obtain the chiral condensate as a function of the temperature. Furthermore, since the quark mass appears in the boundary condition, it is also possible to vary its value, and correspondingly, one gets the function $\sigma(m_q, T)$. We plot the results in Fig. 1. In the upper, middle panels of the figure, the results of models I and II are presented, respectively. For each model, we show two

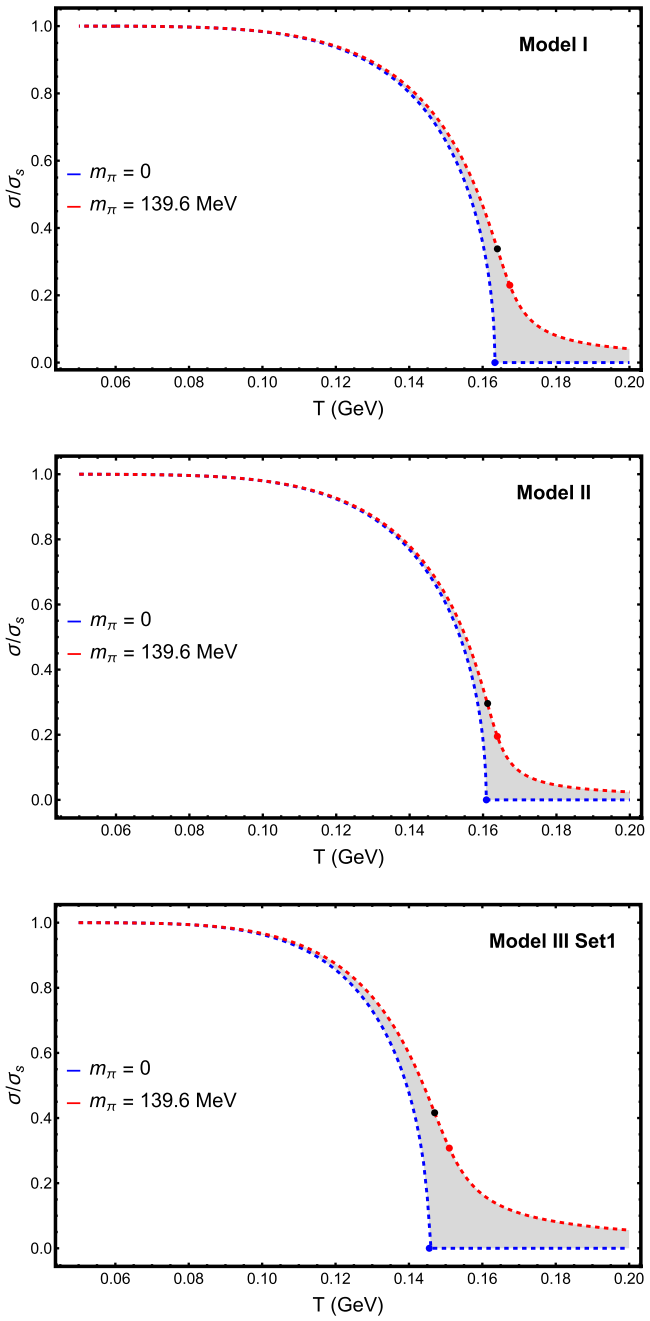

FIG. 1. Chiral phase transitions and the crossover region for different pion masses. The blue line corresponds to the chiral limit $m_\pi = 0$, while the red line is for the physical pion mass ($m_\pi = 139.6$ MeV). The shaded gray area highlights the region between these two curves. Blue dots mark second-order phase-transition points; black and red dots indicate the pseudocritical temperatures obtained from the maxima of $|d\sigma/dT|$ and the chiral susceptibility, respectively.

different cases, with a physical quark mass and in the chiral limit. For the physical case, we tune the quark mass to get a pion mass of around 139.6 MeV, while in the chiral limit, we take $m_q = 0$ and correspondingly $m_\pi = 0$ for its

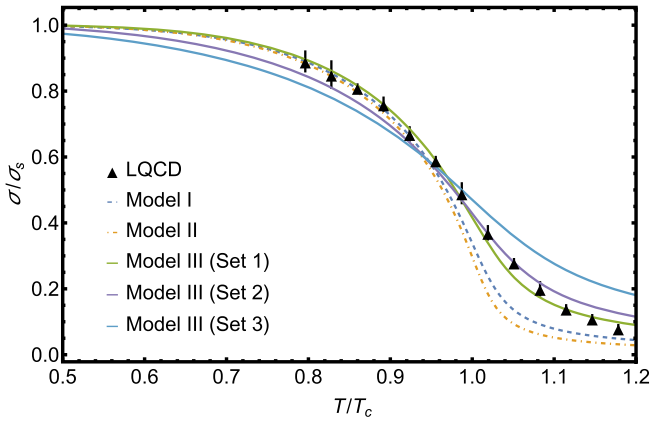

FIG. 2. The variation of the normalized chiral condensate with T/T_c computed and compared with the lattice-QCD simulation results represented by black triangles with error bars, as reported in Ref. [6].

Goldstone nature. The vacuum values of the condensate σ_s and the second-order transition temperature are $\sigma_s = 0.01475\ \mathrm{GeV}^3$, $T_{c0} = 163.3$ MeV for model I, and $\sigma_s = 0.02749\ \mathrm{GeV}^3$, $T_{c0} = 160.9$ MeV for model II. For the physical quark masses, the pseudocritical temperatures extracted from the maxima of $|d\sigma/dT|$ are $T_c = 164.0$ MeV for model I and $T_c = 161.2$ MeV for model II, while those from the maxima of the chiral susceptibility are $T_c = 167.4$ MeV for model I and $T_c = 163.9$ MeV for model II (red dots). To eliminate the influence of other differences between the models, we plot the chiral condensate σ/σ_s (where σ_s is the zero-temperature condensate) as a function of T/T_c across all the models, alongside lattice-QCD data (the filled black triangles) from Ref. [6], as shown in Fig. 2. The results reveal a systematic trend: Models I and II (dashed and dotted-dashed lines) track the lattice data reasonably well near the pseudocritical temperature ($T/T_c < 1$), but deviate significantly in the high-temperature crossover region ($T/T_c > 1$). We explored parameter variations to improve the agreement, but the effect was marginal. The main reason is that the crossover transition at the physical quark mass appears too sharp in these two models, as illustrated in the figures, exhibiting an overly rapid decrease of the chiral condensate at high temperatures.

To broaden the transition region, we note that the chiral condensate in the soft-wall model is sensitive to the quartic coupling. As demonstrated in Ref. [47], a stronger quartic coupling term suppresses the chiral condensate more significantly at low temperatures. Specifically, if one introduces a quartic coefficient that depends on the coordinate r (induced by its coupling to the dilaton) and allows it to grow with increasing r, the low-temperature condensate is suppressed more strongly than its high-temperature counterpart. Furthermore, softening the potential at large χ (e.g., by including a logarithmic term) enables the condensate to approach its $T = 0$ limit more gradually. The interplay between these two mechanisms is expected to effectively broaden the temperature profile of the condensate. Motivated by this insight, we propose a refined model formulation, defined as follows:

TABLE III. Fitting parameters in model III.

Parameters	m_{phy} (MeV)	μ_g (MeV)	μ_c (GeV)	b	a_0	a_1	a_2
Set 1	1.61	0.40	1.30	1	250	5	0.02
Set 2	1.14	0.25	1.30	10	250	5	0.02
Set 3	3.10	0.22	1.15	50	20	5	0.20

$$\begin{aligned}\text{Model III:}\ V(\chi) &= \frac{1}{2}m_5^2\chi^2 + \frac{1}{2}\lambda(r)\chi^2\ln(1+b\chi^2),\\ m_5^2(r) &= -3 - \mu_c^2 r^2,\\ \lambda(r) &= a_0 - a_1\tanh(a_2 r^2).\end{aligned} \tag{13}$$

We will call this model "model III." As can be seen from the setup of these models, in addition to μ_g, which accounts for linear confinement [38], an additional scale is required to describe spontaneous chiral-symmetry breaking [42].

Upon selecting parameter set 1 of model III from Table III and solving the equations of motion, we obtain the chiral condensate in this model. As illustrated in the bottom panel of Fig. 1 and the green solid line in Fig. 2, model III (set 1) yields a broader crossover region, as expected. Compared to the other two models, model III with parameter set 1 (green solid line) achieves substantially better agreement with lattice-QCD results across the entire temperature range. It confirms that the functional form of the scalar potential itself—specifically, the logarithmic correction and r dependence in model III—is essential for capturing the quantitative thermodynamics of the chiral crossover. For later convenience, we also obtain the vacuum condensate σ_s and the second-order transition temperature T_{c0} for model III set 1 as $\sigma_s = 0.002918\ \mathrm{GeV}^3$, $T_{c0} = 145.5$ MeV. Correspondingly, for physical quark masses, the pseudocritical temperature extracted from the maxima of $|d\sigma/dT|$ is $T_c = 147.0$ MeV for model III set 1 (black dots), while that from the maxima of the chiral susceptibility is $T_c = 151.5$ MeV for model III set 1 (red dots).

The broadening of the crossover region, which helps describe the lattice data at the physical quark mass in model III set 1, is also important for investigating scaling behaviors, particularly the T_c–m scaling. Since the primary objective of this work is to rigorously investigate these scaling behaviors, we introduce two additional parameter sets denoted as sets 2 and 3 (listed in Table III), which produce even broader crossover regions and provide a systematic assessment of how the crossover region affects the T_c–m scaling, as discussed in the following sections. As shown in the purple solid line in Fig. 2, model III set 2

produces a mild broadening of the phase transition region. Qualitatively, its deviation from the lattice-QCD data remains approximately within 1σ for $T < 1.1T_c$ (with only a few data points slightly exceeding this bound). It should be emphasized that the "1σ" bound referred to here is a qualitative description rather than a rigorously defined statistical quantity. As shown in the blue solid line in Fig. 2, model III set 3 exhibits a larger deviation, remaining approximately within 5σ for $T < 1.1T_c$. We qualitatively regard this as an upper bound on the effect of broadening the phase transition region. For later convenience, we also obtain $\sigma_s = 0.001688\ \mathrm{GeV}^3$, $T_{c0} = 163.1$ MeV for set 2, and $\sigma_s = 0.002175\ \mathrm{GeV}^3$, $T_{c0} = 144.4$ MeV for set 3.

In summary, we have shown that the soft-wall model, with appropriate modifications, can accurately describe the chiral phase transition at the physical quark mass. Based on this, we will proceed to study the scaling properties in the subsequent sections.

III. SCALING FUNCTIONS IN THE HOLOGRAPHIC MODEL

As discussed in the last section, with arbitrarily small quark mass, the chiral phase transition turns into a crossover. When the transition point lies sufficiently close to the critical point, it can be strongly influenced by the critical point. A scaling window and universal scaling behavior appear in this region, which might be relevant to the search for the CEP of the QCD phase diagram if the CEP belongs to the same universality class. In this context, it has been verified that the chiral condensate near the critical point obeys the following scaling laws:

$$\sigma(T, m_q = 0) \sim (T_{c0} - T)^{\beta}, \quad \sigma(T_{c0}, m_q) \sim m_q^{1/\delta}, \tag{14}$$

with $\beta = 1/2$ and $\delta = 3$ in the two-flavor limit [47]. However, these scaling laws capture the critical behavior only along certain directions, namely, holding m_q fixed for β and T fixed for δ. To get more information about how the critical point governs the crossover region, one has to extract the scaling functions. This section is therefore devoted to their determination.

A. Scaling functions

The theoretical derivation of the universal scaling near a critical point can be easily found in a standard textbook [63] of statistical physics. Taking a spin system as an example, the order parameter or the magnetization M obeys the scaling law

$$M = h^{1/\delta} f_G(z), \tag{15}$$

where $f_G(z)$ is the scaling function, h is the source of the magnetization, and z is a scaling parameter defined as

$$z = t/h^{1/\Delta}, \qquad t = (T_{c0} - T)/T_{c0}, \tag{16}$$

with $\Delta = \beta\delta$. If one takes $T = T_{c0}$ or $h = 0$, the scaling law will be reduced to

$$M(t = 0) = h^{1/\delta}, \tag{17a}$$

$$M(h = 0) = t^{\beta}, \tag{17b}$$

which implies the conditions for f_G,

$$f_G(0) = 1 \quad \text{and} \quad f_G(z) \underset{z \to -\infty}{\to} (-z)^{\beta}. \tag{18}$$

In the current model, the critical point locates at $T = T_{c0}, m_q = 0$. It can be numerically checked that the order parameter σ in all three models obeys the following scaling law:

$$\sigma(T = T_{c0}, m_q) = A m_q^{1/\delta}, \tag{19a}$$

$$\sigma(T, m_q = 0) = B(T_{c0} - T)^{\beta} \tag{19b}$$

with A and B two coefficients, which can be numerically extracted. One can take $m_q = 0$ and vary T around T_{c0} to get the near-critical temperature scaling. The results for the three models are given in Fig. 3. It is shown that σ^2 is almost a straight line as a function of T, indicating $\beta = 1/2$. Since the scaling function is a quantity independent of the specific parameter choice, and in order to more clearly compare the T_c scaling behavior of other holographic models in subsequent discussions, all results for model III presented in this section are obtained using parameter set 3, which yields a broader crossover region. By fitting the slope of the straight lines, one can get the coefficient A as listed in Table IV. Similarly, one can take $T = T_{c0}$ and vary m_q around $m_q = 0$. It is found that in this case σ^3 is almost lying in a straight line as a function of m_q. Thus, one gets $\delta = 3$. The coefficient B can be obtained numerically, and we list the result in Table IV. In fact, those quantities can also be extracted analytically. Please refer to [47] for the details.

To obtain the more general scaling function $f_G(z)$, we follow the convention of [64] and define the magnetization as $M = \sigma/\sigma_0$, the source h as $h = m_q/m_0$, and $t = (T_{c0} - T)/T_{c0}$. After that, we get

$$M(t = 0, h) = \frac{A h^{1/\delta} m_0^{1/\delta}}{\sigma_0}, \tag{20a}$$

$$M(t, h = 0) = \frac{B t^{\beta} T_{c0}^{\beta}}{\sigma_0}. \tag{20b}$$

Then we get the scaling function $f_G(z)$ as $f_G(z) = M/h^{1/\delta}$. By substituting the condition from Eq. (17) back into

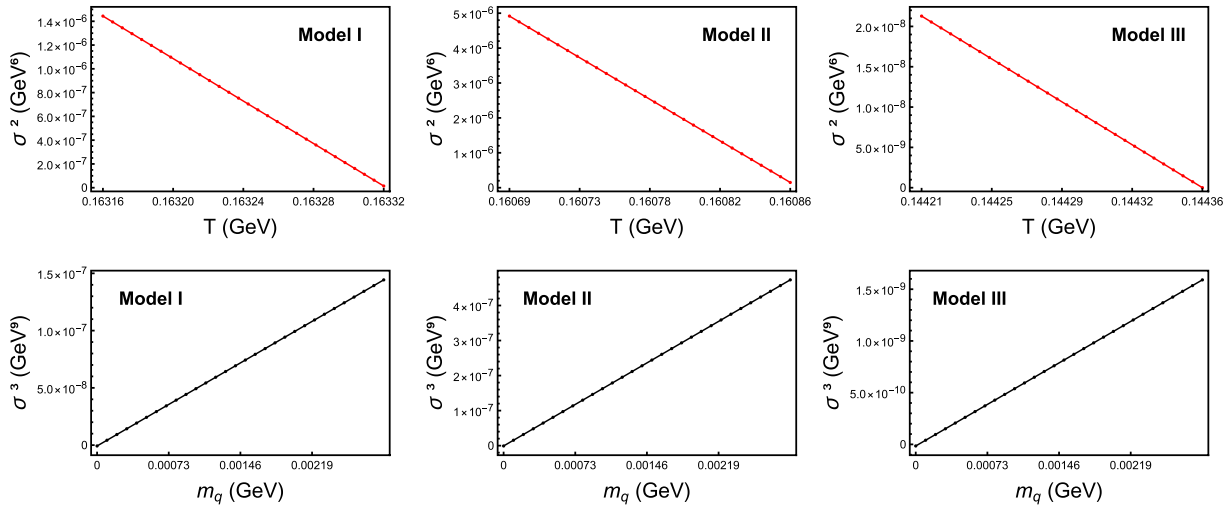

FIG. 3. Critical scaling behavior near the critical point across different models. Red and black symbols are numerical data from the three models; lines are fits.

Eq. (20), we can solve for m_0 and σ_0, and then get the numerical results for $f_G(z)$. We will discuss the numerical results in the next subsection.

In the literature, another scaling function $f_\chi(z)$ is widely studied. It is defined from the chiral susceptibility χ_M as

$$\chi_M = \frac{\partial M}{\partial h} = \frac{h^{1/\delta-1}}{m_0} f_\chi(z), \tag{21}$$

which can be extracted from the near-critical values of chiral susceptibility in terms of the chiral condensate,

$$\chi_M = \frac{m_0}{\sigma_0}\chi_\sigma = \frac{m_0}{\sigma_0}\frac{\partial \sigma}{\partial m_q}. \tag{22}$$

Here, although χ_σ can be extracted by numerically differentiating σ with respect to m_q, it can be directly extracted by performing a perturbative analysis of Eq. (8). If one gets a solution χ_0 at a given temperature T and m_q, a small variation δm_q in the quark mass will induce a variation $\delta\chi$ in χ_0. Then, it is easy to derive the equation of motion for $\delta\chi$ as

$$\delta\chi'' + \left(3A' + \frac{f'}{f} - \phi'\right)\delta\chi' - \frac{e^{2A}}{f} V_{\chi\chi}(\chi_0)\delta\chi = 0. \tag{23}$$

TABLE IV. The extracted values of A and B as determined by various models.

Model	$A(\mathrm{GeV}^{8/3})$	B (GeV^2)
Model I	0.0367383	0.0935534
Model II	0.0545202	0.172141
Model III	0.00818794	0.0121398

As in the above discussion, we can obtain the expansion of $\delta\chi$ at $r = 0$ and $r = r_h$ as

$$\delta\chi(r \to 0) = \delta m_q \zeta r + \cdots + \frac{\delta\sigma}{\zeta} r^3 + \mathcal{O}(r^4), \tag{24a}$$

$$\delta\chi(r \to r_h) = 1 - \frac{V''(c_0)}{4r_h}(r - r_h) + \mathcal{O}(r - r_h)^2. \tag{24b}$$

Then, using the same shooting method as in Sec. II, one can obtain $\delta\sigma$ as a function of δm_q for given temperatures. Thus, the chiral susceptibility can be obtained as $\chi_\sigma = \delta\sigma/\delta m_q$. We will discuss the numerical results later. Before that, we note that the scaling functions f_G and f_χ have a general relation. Performing the differentiation with respect to m_q, it is not difficult to get

$$f_\chi(z) = \frac{1}{\delta} f_G(z) - \frac{z}{\beta\delta} f'_G(z). \tag{25}$$

Considering the case $T = T_{c0}$, Eqs. (15) and (21) yield that the ratio between the two scaling functions approaches a constant near the critical point, i.e.,

$$\frac{f_\chi(0)}{f_G(0)} = \frac{1}{\delta}. \tag{26}$$

The above relations are quite general for different systems. Thus, a self-consistent holographic model should produce results obeying those constraints. We will check the numerical results from the soft-wall model in the next section.

B. Numerical scaling functions from the soft-wall AdS/QCD models

With the preparations described above, we numerically extract the scaling functions in the soft-wall AdS/QCD models. First, we obtain the numerical data for the chiral condensate σ near the critical point (T near T_{c0} and m around 0). Then, from Eqs. (15) and (20a), we can extract the results of $f_G(z)$. The numerical results of the three models and the comparison with the mean-field result from Ref. [65] are presented in Fig. 4. For each case, we take $m_q = 0.1, 0.2, 0.3$ MeV as examples. It can be seen that for all models the scaling function $f_G(z)$ approaches the mean-field result (the black solid lines) from [65] when the quark mass approaches the chiral limit. It can be checked that $f_G(0) = 1$ for all models, consistent with the definition. In the range of $-2 < z < 5$, all three models merge with mean-field results together. But in the range of $-5 < z < -2$, the results in models I and II converge much faster to the mean field, while for model III it is slower and agrees with the mean-field result only when m_q is of order 10^{-2} MeV $f_G(z)$ (that is why we add $m_q = 0.01, 0.03, 0.05$ MeV for model III). It is not difficult to understand this behavior, as the increase in m_q will drive the system away from the critical point, resulting in a violation of the scaling behavior. However, it appears that the scaling window for model III is smaller than the other two models. Later, we will see the impact of this in the scaling of the pseudocritical temperatures.

As a check of the consistency of the model, we also examine the behavior of $f_G(z)$ as z approaches $-\infty$. It is shown in Fig. 5 that when z decreases to -8, in the three models, $f_G(z)$ can be well described by $(-z)^{1/2}$. From these calculations, we confirm that the full critical scaling of the soft-wall AdS/QCD models is governed by the mean-field scaling. To construct a more realistic model, we also compare the scaling function in model III with the lattice results for the $O(4)$ model in Fig. 6. From the figure, obvious deviations of the model results from the lattice results appear in the range of $z < -1$ and $z > 1$. Though the scaling function is defined at the critical point, for later discussion, we also present a direct extension through Eqs. (15) and (20a) to $m_q = 0.01, 0.3, 1$ MeV and the physical point. Interestingly, the extended scaling function bends toward the lattice results in the region of negative z. As the quark mass slightly increases, part of the scaling function gradually shifts toward the $O(4)$ behavior observed in lattice QCD [66,67]. By comparison, the other two soft-wall models yield scaling functions that remain valid over a broader range as the quark mass changes. This might help improve the temperature scaling within the framework of the soft-wall model, which can be seen in the later discussion.

For the scaling function f_χ, as mentioned in the previous section, it can be obtained in two different ways. First, we can directly extract it through the general relation Eq. (25). The results in model III are given in Fig. 7, compared with the lattice simulation of Ref. [16]. From the figure, we obtain $f_\chi(0) \simeq 0.322$. From Eq. (26), this value should be $f_\chi(0) = \frac{1}{\delta} f_G(0) = \frac{1}{3}$. The deviation from this exact value is mainly from the numerical errors, due to the complexity of directly taking $m = 0$ (instead, we take a tiny but finite value). It can also be seen that a peak with its center at $z = 1.115, f_\chi^{\max} = 0.406$ appears in the curve for f_χ. The ratio $f_\chi(z = 0)/f_{\chi,\max}$ is approximately equal to 79%. Later, we will see an interesting connection between this

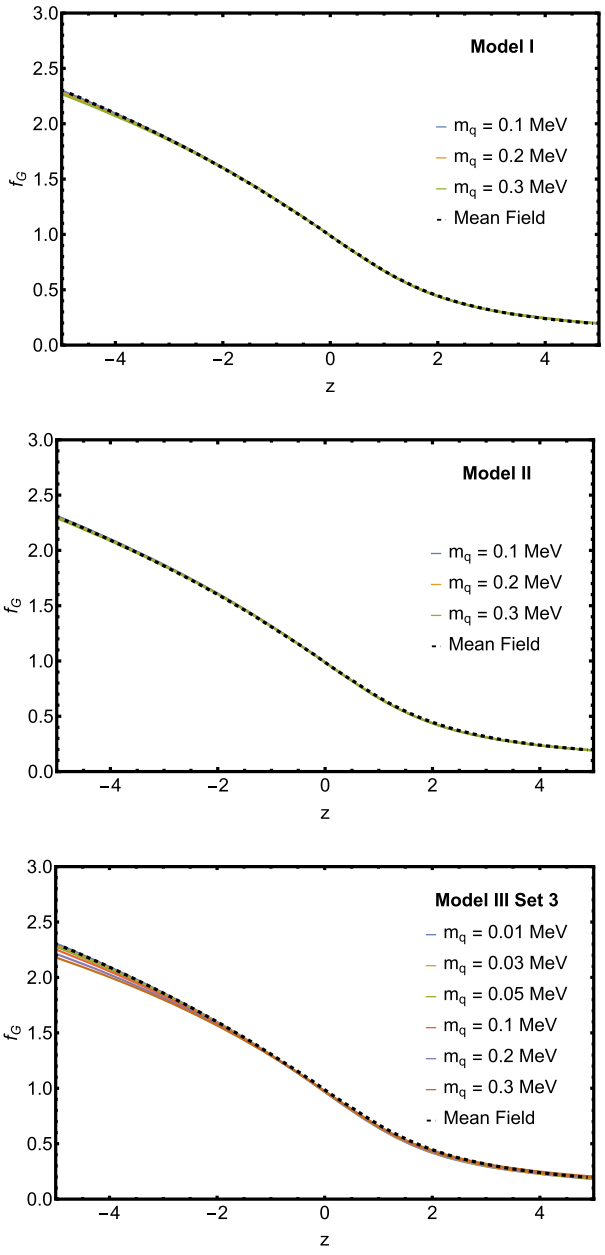

FIG. 4. Scaling function $f_G(z)$ for the three holographic models at several finite quark masses, together with the mean-field result (black solid line) taken from Ref. [65].

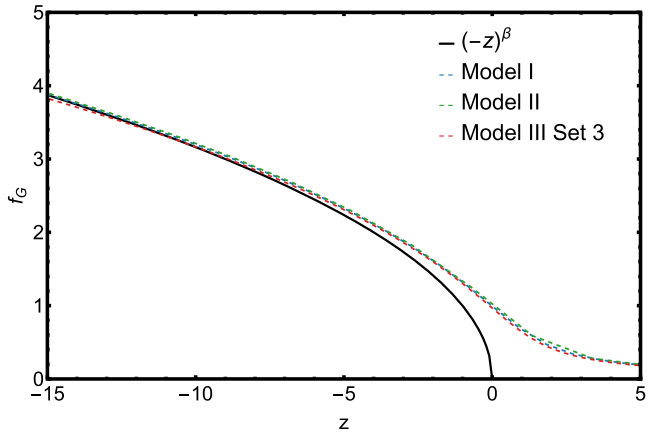

FIG. 5. The asymptotic fitting of the scaling function f_G to $(-z)^{\beta}$ as $z \to -\infty$. The quark mass is set to $m_q = 0.01$ MeV for all three models.

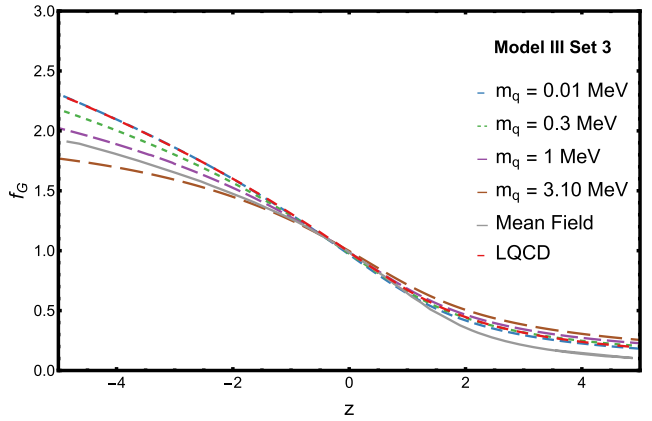

FIG. 6. A comparison of the scaling function obtained from model III set 3 with those derived from the mean-field approximation [65] (the red dashed line) and lattice-QCD simulations for $O(4)$ model [66,67] (the gray solid line).

ratio and the temperature scaling behavior. Since the holographic computation is restricted to the mean-field approximation, its prediction for f_χ cannot quantitatively agree with any of the lattice results obtained for the O(4), O(2), or Z(2) universality classes. The underlying scaling relations are nevertheless respected; all differences stem solely from the distinct critical exponents.

We can also obtain f_χ from the chiral susceptibility through Eq. (21). Figure 8 presents the computed f_χ from various models in this way, compared to the theoretical predictions obtained from Eq. (25). From the figure, we can see that the results obtained from the two methods are almost the same when the quark masses are very small. Thus, the general relation between f_G and f_χ is satisfied in the soft-wall model. Notably, model III displays a stronger dependence on the quark mass, while models I and II exhibit relatively minor changes in their scaling functions.

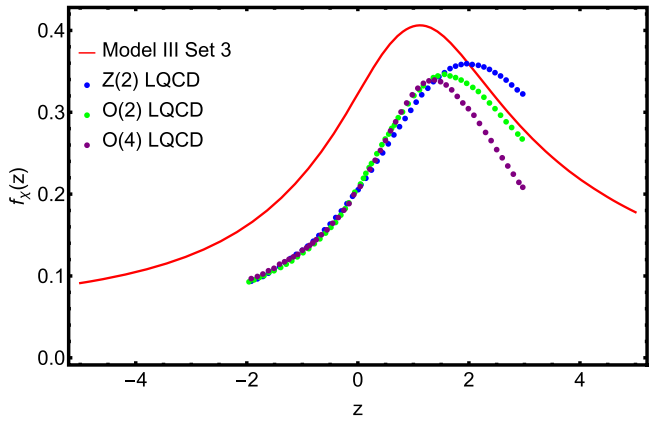

FIG. 7. A comparison of the scaling function $f_\chi(z)$ from model III set 3, with the corresponding results derived from lattice QCD in the $O(2)$, $Z(2)$, and $O(4)$ universality classes [16].

This suggests that, under the mean-field approximation, variations among models may lead to different scaling regions.

In a short summary, all the soft-wall models obey the same scaling behavior. The obtained scaling functions are the same for various models. However, when extended to finite quark masses, the scaling functions might show a slight dependence on the quark mass, and the scaling region might be different for different models.

IV. TC SCALING BEHAVIOR UNDER THE CHIRAL PHASE TRANSITION

As already mentioned in the above sections, by taking a tiny but finite quark mass, the chiral phase transition turns from a second-order transition into a continuous crossover. Although the continuous crossover is not a real phase transition, it is a smooth and rapid change between two different phases, and one can define a pseudocritical temperature in different ways. Generally, the pseudocritical temperature also obeys a certain kind of scaling law. In this section, we will investigate the scaling behavior of the transition temperature.

A. Chiral order parameters

Several kinds of chiral order parameters can be used in a pseudotransition. For the holographic calculation, two of them are suitable for extracting the transition temperature. One of them is defined from the peak of the derivative with temperature $|d\sigma/dT|$, while the other is from the peak of the chiral susceptibility defined as $\chi_\sigma = \frac{\partial\sigma}{\partial m_q}$.

According to Ref. [68], although the chiral order parameters differ, the extracted pseudocritical temperatures differ only slightly, whereas Ref. [69] shows that different chiral order parameters can lead to much larger discrepancies in pseudocritical temperature. To study the impact of the chiral order parameters, we take two different cases in

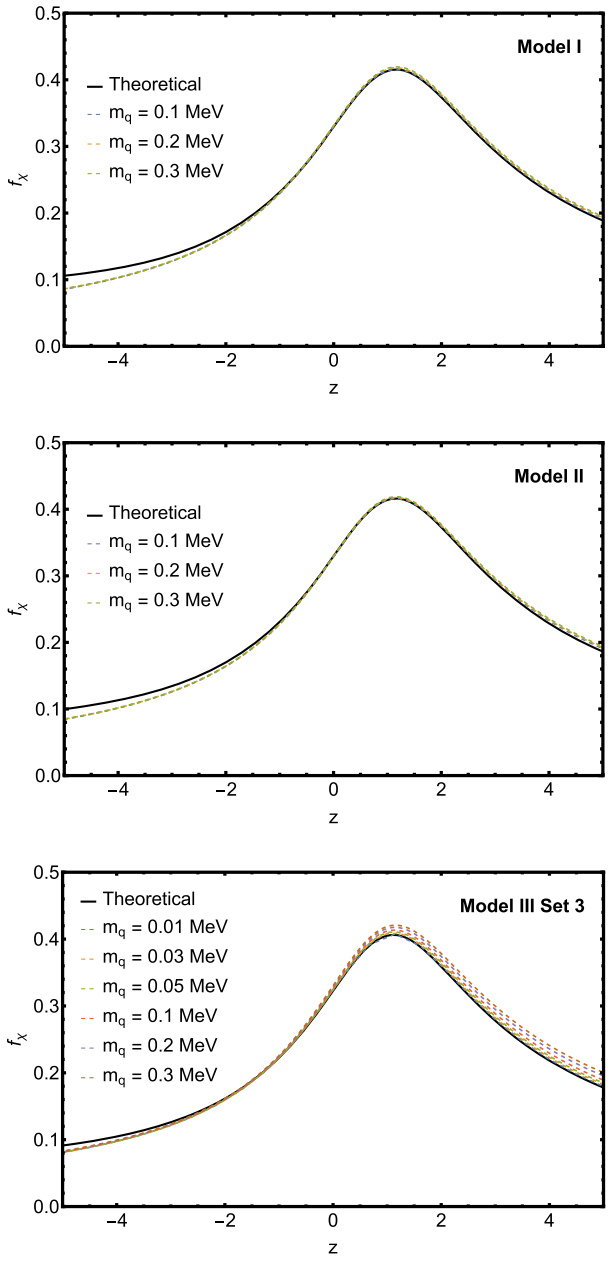

FIG. 8. The dependence of the scaling function f_χ on the quark mass. The solid curve denotes the theoretical prediction extracted from f_G through Eq. (25), whereas the dashed curves illustrate the scaling functions for various quark masses.

model III set 3 with $m_q = 0.059$ MeV, $m_\pi = 20$ MeV and $m_q = 3.63$ MeV, $m_\pi = 150$ MeV as examples. As shown in Fig. 9, we can extract T_c by identifying the temperatures corresponding to the peaks of the two different chiral order parameters. With $m_q = 0.059$ MeV, as shown in the blue curves, the peak of $|d\sigma/dT|$ locates at $T_{c,\sigma} = 0.1444$ GeV with a height of $H_\sigma = 13.83$, which are very close to $T_{c,\chi} = 0.1451$ GeV, $H_\chi = 14.42$. As for $m_q = 3.63$ MeV, both the peak location and its height obtain larger

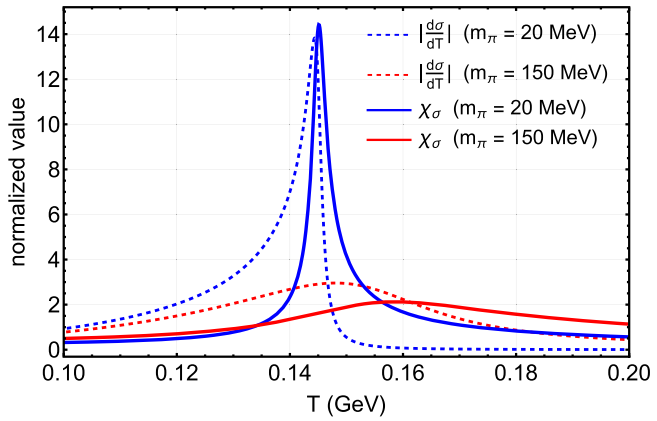

FIG. 9. The critical temperatures T_c from chiral susceptibility and chiral condensate, with $m_\pi = 150$ MeV and $m_\pi = 20$ MeV. The normalized value denotes each susceptibility scaled by the mean of all susceptibilities.

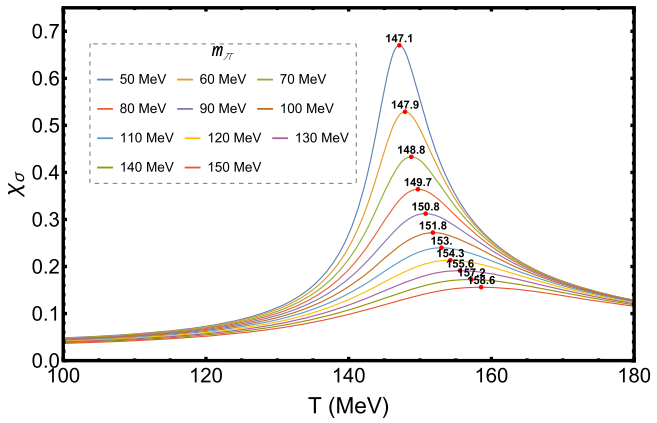

FIG. 10. Chiral susceptibility for various pion masses in model III set 3.

differences, with $T_{c,\sigma} = 0.1481$ GeV, $H_\sigma = 2.96$ and $T_{c,\chi} = 0.1586$ GeV, $H_\chi = 2.13$.

Similar calculations can be imposed for the other values of the quark mass. To show the tendency of the chiral susceptibility, we give the results for various pion masses from model III set 3 in Fig. 10. From the figure, we can see that when the quark mass increases, the height of the peaks of χ_σ decreases, while the pseudocritical temperature (the peak location) increases. We also present the results of the pseudocritical temperatures for all three models in Fig. 11. We observe that the critical temperatures obtained from the two different order parameters differ significantly at high temperatures, with the one from the chiral susceptibility being much more sensitive to the pion mass. Generally, the transition temperatures from the chiral susceptibility are higher than those from $d\sigma/dT$ with the same quark mass. It is self-consistent that the differences of the two transition temperatures vanish toward the chiral limit, when the

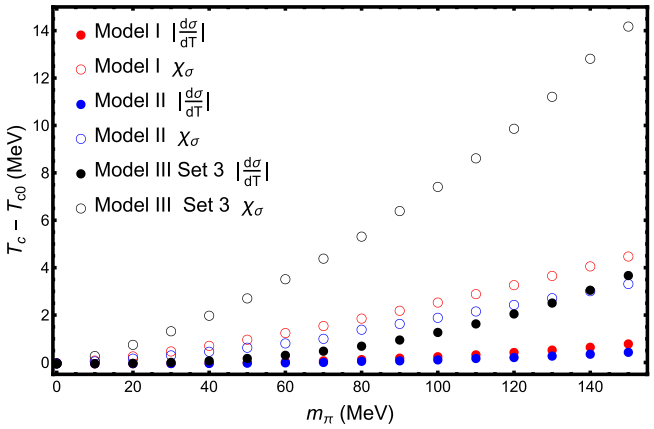

FIG. 11. The pseudopion mass varies with different chiral order parameters and the temperature of the phase transition. The open circles represent the critical temperatures extracted using the chiral condensate as the order parameter, while the solid circles correspond to those obtained from the chiral susceptibility. All temperatures are shifted by subtracting the pseudocritical temperature T_c in the chiral limit.

transition becomes a rigorous one and an exact transition temperature can be defined. For the effect of the model setting, it is easy to see that both transition temperatures from the two order parameters in model III are more sensitive to the pion mass than those in models I and II. In fact, this is why we adopt the model proposed in this work to study the dependence of the critical temperature, extracted from the chiral susceptibility, on both the quark mass and the pion mass. Since the chiral susceptibility is widely used in both functional renormalization group calculations and lattice QCD, we will identify the pseudocritical temperature T_c with the maximum ($\chi_\sigma^{\max}$) of the chiral susceptibility in later calculations, in order to give a straightforward comparison with the other methods.

B. T_c scaling

Generally, with a small value of quark mass, the physics near the transition temperature is still governed by the critical scaling behavior. Thus, for small quark masses, the corresponding pseudocritical temperature also obeys a scaling law as

$$T_c = \alpha \times m_q^{1/\Delta} + T_{c0}, \tag{27}$$

with $\Delta = \beta\delta$, T_{c0} the critical temperature in the chiral limit, and α a coefficient depending on the models. This scaling law can be derived from the near-critical scaling of σ. Since the holographic model gives the mean-field critical exponents $\beta = 1/2$, $\delta = 3$, we have $\Delta = 3/2$. As proved in [37], the Gell-Mann-Oakes-Renner relation $m_\pi^2 f_\pi^2 = 2m_q\langle\bar{q}q\rangle$ is satisfied in the soft-wall model; thus, we have $m_\pi^2 \propto m_q$ and $T_c = m_\pi^{4/3} + T_{c0}$.

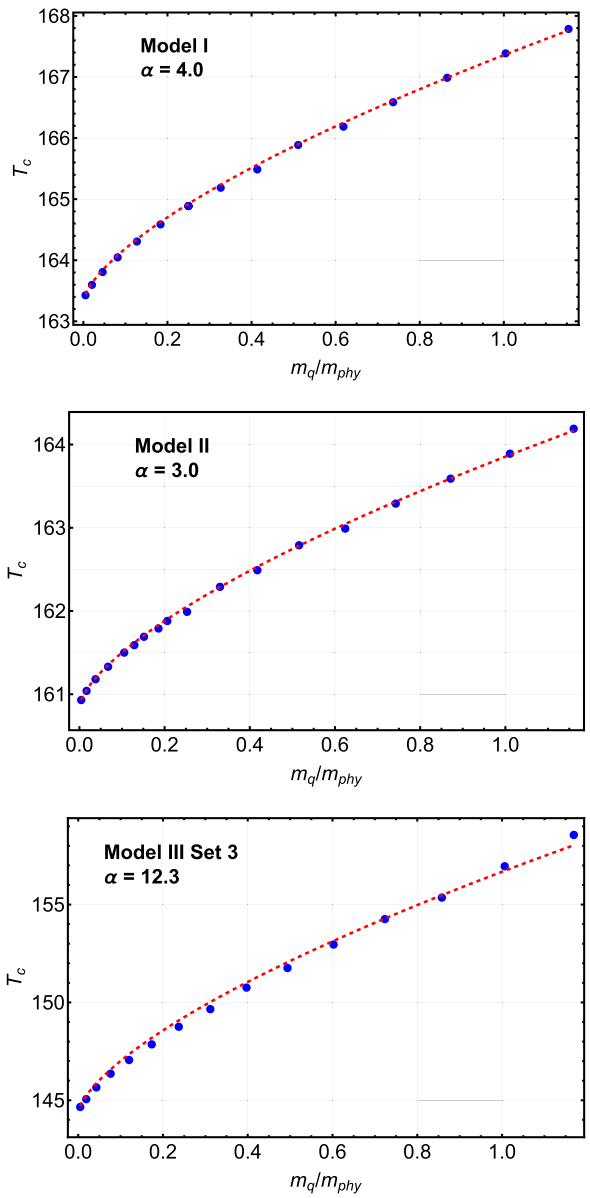

FIG. 12. The dependence of the pseudocritical temperature T_c on the scaled quark mass m_q/m_{phy}, with the physical quark mass m_{phy} corresponding to $m_\pi = 139.6$ MeV. The red dashed curve represents the fit obtained using the data points.

As an explicit check of this scaling behavior, we extract the pseudocritical temperatures as functions of the quark mass for the three models, as shown in the blue dots in Fig. 12. The upper, middle, and lower panels show the results in models I, II, and III, respectively. There, we show that the pseudocritical temperatures can be well described by the scaling law (the red dashed lines) with $\alpha = 4.0$ for model I, $\alpha = 3.0$ for model II, and $\alpha = 12.3$ for model III, with T_{c0} taking the values in the chiral limit of the corresponding models. From the fitting, it is interesting to see that the "slope" α in model III set 3 is much larger than that in models I and II.

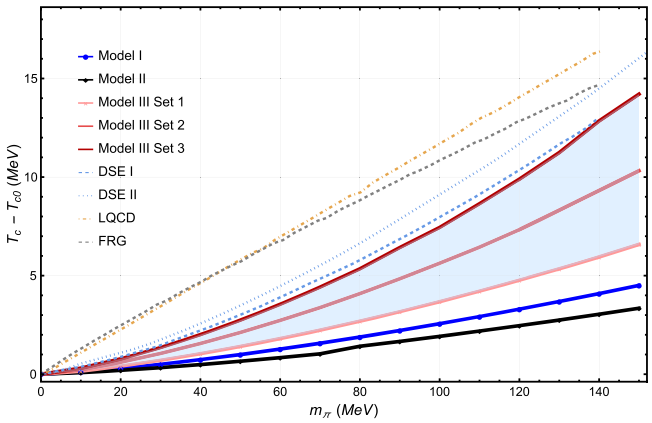

FIG. 13. The pseudocritical temperature as a function of m_π for different models. The lattice-QCD results are taken from Ref. [16], the FRG results are taken from Ref. [70], and the DSEs approach results are taken from Ref. [9].

In Fig. 13, we present the results for the pseudocritical temperature T_c as a function of the pion mass. Because of the limited availability of $N_f = 2$ data, we take the $N_f = 2 + 1$ results from lattice QCD (the orange-brown dot-dashed line, from [16]), FRG (the medium gray dashed line, from [70]), and DSE approaches (the light blue dashed line and light blue dotted line, from [9]) for comparison. We have subtracted the T_c data from T_{c0} in order to get rid of the effect of differences in T_{c0}. From the figure, it can be seen that, unlike the LQCD and FRG results, our model does not exhibit a linear dependence. The linear dependence observed in the FRG and LQCD results is because their critical exponents are beyond the mean-field level of the 3D $O(4)$ universal class. Here we show the T_c-scaling blue band corresponding to different parameter choices in model III. It is evident that, in the case of the largest values, our results approach those obtained from the DSE analysis.

Besides the match of scaling exponent Δ with the DSE results for all three models, it is obvious that the increasing rates in models I and II are too small compared with the DSE results, as well as the lattice simulations. However, by doing a further modification to the scalar potentials, we find a way to cure this problem in model III. The logarithmic term and the r-dependent coupling in the scalar potential soften the potential, thereby broadening the continuous transition and making the scaling slope steeper. This is why we try to propose a new modification to the soft-wall model. We note that the scaling of T_c should be taken into account in model construction within the soft-wall framework. It is important to clarify, however, that the primary goal of this work is to demonstrate the qualitative capability of model III, rather than to present a finalized, perfectly optimized parameter set. The three parameter sets of model III represented by the blue band in Fig. 13 demonstrate that model III has the potential to achieve T_c scaling results closer to those of lattice QCD and DSE.

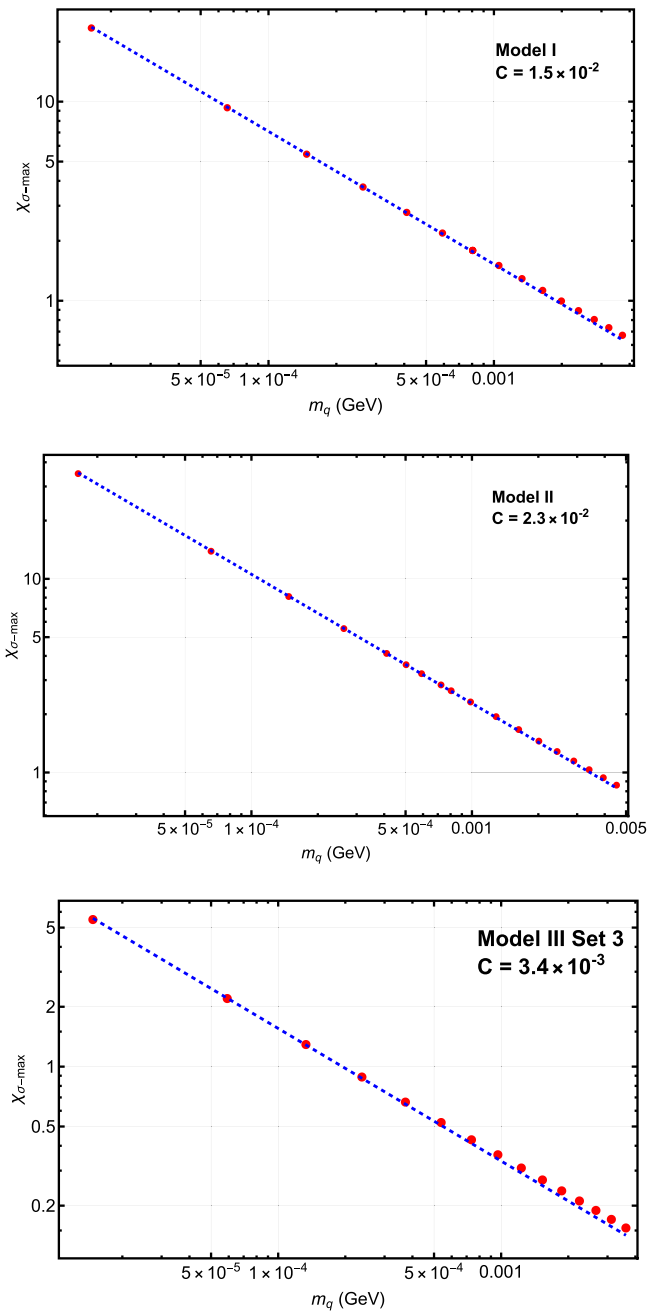

FIG. 14. Dependence of the maximum chiral susceptibility $\chi_{\sigma,\max}$ on the quark mass.

Furthermore, in Fig. 14 we show the relation between the maximum chiral susceptibility $\chi_{\sigma,\max}$ and m_q. According to Ref. [71], they obey the following scaling behavior:

$$\chi_{\sigma,\max} = C \times m_q^{1/\delta-1}. \tag{28}$$

It can be seen from the figure that the scaling law (the blue dotted lines) fits the numerical data quite well. The coefficient C is fitted as $C = 0.015$ for model I, $C = 0.023$ for model II, and $C = 0.0034$ for model III set 3.

Again, we see that the coefficient in model III set 3 has a different order from models I and II, which might be important in improving the T_c scaling with pion mass.

Therefore, we have seen that all the scaling laws are satisfied in the soft-wall AdS/QCD models, though all the exponents are at the mean-field level. It can also be seen that the models with a simple power of the scalar potential cannot well describe the coefficients (or the slopes). We propose a way to improve this behavior and get comparable T_c scaling in both the exponents and the coefficients, with those obtained from the other nonperturbative methods.

C. The transition temperature toward the chiral limit

Before closing this section, we will discuss another interesting topic. As we know, it is more expensive for lattice simulations to work with a smaller quark mass. In particular, it is very hard in the chiral limit. Thus, different ways have been developed to extrapolate the finite quark-mass calculation to get reliable results in the chiral limit. To get the critical temperature in the chiral limit at a lower cost, it is better to find certain observables from which the critical temperatures converge to that in the chiral limit more rapidly. As shown in lattice simulations [16], the ratio $R = f_\chi(z=0)/f_{\chi,\max}$ coincides with the ratio of the chiral susceptibility evaluated at the critical temperature in the chiral limit to its peak value, i.e., $\chi_\sigma(T=T_{c0})/\chi_{\sigma,\max} = f_\chi(z=0)/f_{\chi,\max} = R$ for small quark masses. Such a conclusion comes from the fact that the pseudocritical temperatures for small quark masses are governed by the critical point and thus controlled by f_χ as well ($z=0$ characterizes the critical point). A direct consequence of this relation is that T_{c0} can be obtained from calculations at finite quark masses from the condition $\chi_\sigma(T=T_{c0}) = R\chi_{\sigma,\max}$ (here, we note that there are two temperatures satisfying this condition, and one has to choose the lower one). In this section, we provide explicit holographic confirmation of this relation.

From the previous discussion, we have $R = f_\chi(0)/f_{\chi,\max} \simeq 79\%$ in the soft-wall model. Thus, T_{c0} is expected to correspond to the 79% height of the peaks at finite quark masses. As an explicit check, in Fig. 15, we compare the temperatures corresponding to the peak of χ_σ (the blue solid line) for different pion masses with those obtained from the 79% height of the peak (the black dots), in reference to our critical temperature T_{c0} (the red dashed line). The figure clearly shows that the percentage-temperature T_{percent} approaches T_{c0} much faster than T_c. For $m_\pi < 60$ MeV, T_{percent} almost reaches T_{c0}, while $T_c = T_{c0}$ only in the chiral limit $m_\pi = 0$. Here, although we have so far presented results only for model III set 3, we have checked that the relation holds in models I and II as well. Therefore, the holographic calculation confirms that the percentage temperature is a good observable for extracting T_{c0} from finite quark-mass calculations.

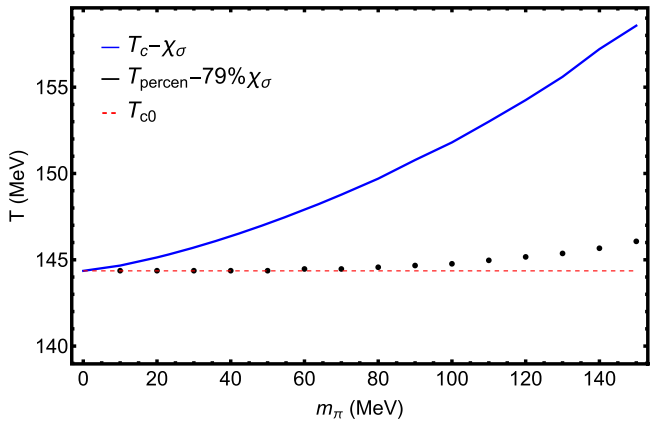

FIG. 15. The relation between the pion mass m_π and the temperature at which χ_σ reaches 79% of its maximum value.

V. CONCLUSION AND DISCUSSION

The critical point of the two-flavor soft-wall AdS/QCD model is systematically studied in Ref. [47], and it is proved to exhibit mean-field scaling laws with exponents $\beta = 1/2$, $\delta = 3$, when tuning either the temperature or the quark mass in its vicinity. However, the universal scaling functions that arise when the temperature and quark mass are varied simultaneously, together with the scaling behavior of the pseudocritical temperature itself, remain largely unexplored in this model. To verify the effectiveness and internal consistency of this holographic model, we present a careful study of the near-critical scaling behavior of various chiral order parameters.

Under different model settings and physical conditions, we find that the rescaled magnetization $M/h^{1/\delta}$ in the chiral limit collapses onto a single, universal curve in the chiral limit $m_q \to 0$, defining the scaling function $f_G(z)$. Quantitatively, this scaling function obtained numerically from holography is in excellent agreement with its four-dimensional mean-field counterpart. Furthermore, we derive a perturbative equation to evaluate the chiral susceptibility, from which we obtain another universal scaling function $f_\chi(z)$. It is found that the universal relationship $f_\chi(z) = \frac{1}{\delta} f_G(z) - \frac{z}{\beta\delta} f_G'(z)$ holds in all three models, confirming the theoretical consistency of this holographic framework.

Furthermore, we extract the pseudocritical temperature from the peak of the susceptibility and from the inflection point of the chiral condensate. In contrast to the claim in Ref. [68], the three models yield markedly different pseudocritical temperatures when extracted from the two order parameters, although the results coincide in the chiral limit. In this context, our results are consistent with the view in Ref. [69], which suggests that different order parameters can yield significantly different pseudocritical temperatures. Adopting the susceptibility-peak definition of the transition temperature, we numerically verify that in

all three holographic models the pseudocritical temperature obeys the universal scaling law $T_c - T_{c0} \sim m_q^{1/\beta\delta}$ or $T_c - T_{c0} \sim m_\pi^{2/\beta\delta}$. The scaling region in these models can extend below the physical quark mass. These findings support the consistency of soft-wall models with mean-field universality. Moreover, we find that the percentage temperature defined by the 79% [the value is set by the ratio $f_\chi(0)/f_{\chi,\max}$], converges to its chiral-limit value much faster than the pseudocritical temperature, offering a practical observable for determining T_{c0}.

While the three holographic models share identical critical exponents and scaling functions in the chiral limit, their scaling coefficients span orders of magnitude. Compared with T_c scaling from DSE [9], FRG [70], and lattice QCD [16], models I and II yield a slope, i.e., the scaling coefficient, that is roughly one third as large, a discrepancy that appears to afflict earlier soft-wall constructions as well. It is interesting to see that by softening the scalar potential with certain logarithmic terms and r-dependent coefficients, model III reproduces a T_c scaling in quantitative agreement with the DSE results [9]. This improvement can be attributed to the logarithmic modification in the scalar potential. While models I and III are equivalent at the critical point (sharing the same subleading expansion), the logarithmic term in model III effectively incorporates higher-order interactions that become relevant for finite quark masses, driving the model toward better agreement with QCD phenomenology. These findings might offer valuable guidance for refining future model constructions in the soft-wall AdS/QCD. It is worth noting that due to the complexity of the numerical computations and the high dimensionality of the parameter space, this work does not present a single parameter set that simultaneously reproduces both the chiral condensate and the T_c scaling with high precision. Nevertheless, we anticipate that future optimization strategies, such as those employing machine learning algorithms, will enable more refined fittings. Finally, in this study, we have restricted our attention to the two-flavor chiral critical point. Extending the analysis to the entire critical lines in the quark-mass phase diagram, and examining the resulting consequences for the critical end point within the same holographic framework, constitutes an interesting direction for future work.

ACKNOWLEDGMENTS

This work is supported by the National Natural Science Foundation of China under Grants No. 12275108 and No. 12235016.

DATA AVAILABILITY

The data that support the findings of this article are not publicly available. The data are available from the authors upon reasonable request.

[1] P. Braun-Munzinger, K. Redlich, and J. Stachel, *Quark-Gluon Plasma 3* (World Scientific, Singapore, 2004), p. 491.
[2] E. Shuryak, Rev. Mod. Phys. **89**, 035001 (2017).
[3] D. H. Rischke, Prog. Part. Nucl. Phys. **52**, 197 (2004).
[4] M. Huang and P. Zhuang, Symmetry **15**, 541 (2023).
[5] R. D. Pisarski and F. Wilczek, Phys. Rev. D **29**, 338 (1984).
[6] S. Borsanyi, Z. Fodor, C. Hoelbling, S. D. Katz, S. Krieg, C. Ratti, and K. K. Szabo (Wuppertal-Budapest Collaboration), J. High Energy Phys. 09 (2010) 073.
[7] M. Cheng *et al.*, Phys. Rev. D **74**, 054507 (2006).
[8] H.-T. Ding, F. Karsch, and S. Mukherjee, Int. J. Mod. Phys. E **24**, 1530007 (2015).
[9] Z. Bai, L. Chang, J. Chao, F. Gao, and Y.-X. Liu, Phys. Rev. D **104**, 014005 (2021).
[10] J. B. Kogut and D. K. Sinclair, Phys. Rev. D **73**, 074512 (2006).
[11] S. Ejiri, F. Karsch, E. Laermann, C. Miao, S. Mukherjee, P. Petreczky, C. Schmidt, W. Soeldner, and W. Unger, Phys. Rev. D **80**, 094505 (2009).
[12] A. Bazavov *et al.*, Phys. Rev. D **85**, 054503 (2012).
[13] F. Burger, E.-M. Ilgenfritz, M. Kirchner, M. P. Lombardo, M. Müller-Preussker, O. Philipsen, C. Urbach, and L. Zeidlewicz (tmfT Collaboration), Phys. Rev. D **87**, 074508 (2013).
[14] A. Y. Kotov, M. P. Lombardo, and A. Trunin, Phys. Lett. B **823**, 136749 (2021).
[15] A. Y. Kotov, M. P. Lombardo, and A. Trunin, Symmetry **13**, 1833 (2021).
[16] H. T. Ding *et al.* (HotQCD Collaboration), Phys. Rev. Lett. **123**, 062002 (2019).
[17] F. Gao and J. M. Pawlowski, Phys. Rev. D **105**, 094020 (2022).
[18] J. Bernhardt and C. S. Fischer, Phys. Rev. D **108**, 114018 (2023).
[19] J. Braun, B. Klein, and P. Piasecki, Eur. Phys. J. C **71**, 1576 (2011).
[20] J. Braun *et al.*, Phys. Rev. D **111**, 094010 (2025).
[21] Z. Fodor and S. D. Katz, Phys. Lett. B **534**, 87 (2002).
[22] G. 't Hooft, Conf. Proc. C **930308**, 284 (1993), arXiv:gr-qc/9310026.
[23] L. Susskind, J. Math. Phys. (N.Y.) **36**, 6377 (1995).
[24] J. M. Maldacena, AIP Conf. Proc. **484**, 51 (1999).
[25] G. Policastro, D. T. Son, and A. O. Starinets, Phys. Rev. Lett. **87**, 081601 (2001).
[26] A. Buchel and J. T. Liu, Phys. Rev. Lett. **93**, 090602 (2004).
[27] P. Kovtun, D. T. Son, and A. O. Starinets, Phys. Rev. Lett. **94**, 111601 (2005).

[28] S. J. Brodsky, G. F. de Téramond, H. G. Dosch, and J. Erlich, Phys. Rep. **584**, 1 (2015).
[29] U. Gursoy, M. Jarvinen, and G. Nijs, Phys. Rev. Lett. **120**, 242002 (2018).
[30] S. S. Gubser, A. Nellore, S. S. Pufu, and F. D. Rocha, Phys. Rev. Lett. **101**, 131601 (2008).
[31] U. Gursoy, E. Kiritsis, L. Mazzanti, and F. Nitti, Phys. Rev. Lett. **101**, 181601 (2008).
[32] D. Li, S. He, M. Huang, and Q.-S. Yan, J. High Energy Phys. 09 (2011) 041.
[33] S. I. Finazzo, R. Rougemont, H. Marrochio, and J. Noronha, J. High Energy Phys. 02 (2015) 051.
[34] R. Zöllner and B. Kämpfer, Eur. Phys. J. Plus **135**, 304 (2020).
[35] Y.-Q. Zhao, S. He, D. Hou, L. Li, and Z. Li, J. High Energy Phys. 04 (2023) 115.
[36] X. Chen and M. Huang, Phys. Rev. D **109**, L051902 (2024).
[37] J. Erlich, E. Katz, D. T. Son, and M. A. Stephanov, Phys. Rev. Lett. **95**, 261602 (2005).
[38] A. Karch, E. Katz, D. T. Son, and M. A. Stephanov, Phys. Rev. D **74**, 015005 (2006).
[39] T. Gherghetta, J. I. Kapusta, and T. M. Kelley, Phys. Rev. D **79**, 076003 (2009).
[40] D. Li and M. Huang, J. High Energy Phys. 11 (2013) 088.
[41] K. Chelabi, Z. Fang, M. Huang, D. Li, and Y.-L. Wu, J. High Energy Phys. 04 (2016) 036.
[42] K. Chelabi, Z. Fang, M. Huang, D. Li, and Y.-L. Wu, Phys. Rev. D **93**, 101901 (2016).
[43] D. Li and M. Huang, J. High Energy Phys. 02 (2017) 042.
[44] S. P. Bartz and T. Jacobson, Phys. Rev. C **97**, 044908 (2018).
[45] Z. Fang, Y.-L. Wu, and L. Zhang, Phys. Lett. B **762**, 86 (2016).
[46] H. A. Ahmed, M. Kawaguchi, and M. Huang, Phys. Rev. D **110**, 046002 (2024).
[47] J. Chen, S. He, M. Huang, and D. Li, J. High Energy Phys. 01 (2019) 165.
[48] F. R. Brown, F. P. Butler, H. Chen, N. H. Christ, Z.-h. Dong, W. Schaffer, L. I. Unger, and A. Vaccarino, Phys. Rev. Lett. **65**, 2491 (1990).
[49] Y. Chen, M. Ding, D. Li, K. Bitaghsir Fadafan, and M. Huang, Phys. Rev. D **111**, 126010 (2025).
[50] M. Lv, D. Li, and S. He, J. High Energy Phys. 11 (2019) 026.
[51] H. Nishihara and M. Harada, Phys. Rev. D **89**, 076001 (2014).
[52] X. Chen, D. Li, D. Hou, and M. Huang, J. High Energy Phys. 03 (2020) 073.
[53] D. Li, M. Huang, Y. Yang, and P.-H. Yuan, J. High Energy Phys. 02 (2017) 030.
[54] D. M. Rodrigues, D. Li, E. Folco Capossoli, and H. Boschi-Filho, Phys. Rev. D **98**, 106007 (2018).
[55] P. Colangelo, J. J. Sanz-Cillero, and F. Zuo, J. High Energy Phys. 11 (2012) 012.
[56] X. Cao, H. Liu, and D. Li, Phys. Rev. D **102**, 126014 (2020).
[57] X. Cao, S. Qiu, H. Liu, and D. Li, J. High Energy Phys. 08 (2021) 005.
[58] X. Cao, M. Baggioli, H. Liu, and D. Li, J. High Energy Phys. 12 (2022) 113.
[59] D. T. Son and M. A. Stephanov, Phys. Rev. Lett. **88**, 202302 (2002).
[60] A. Cherman, T. D. Cohen, and E. S. Werbos, Phys. Rev. C **79**, 045203 (2009).
[61] J. P. Boyd, *Chebyshev and Fourier Spectral Methods* (Courier Corporation, New York, 2001).
[62] W. Liang, X. Cao, H. Liu, and D. Li, Phys. Rev. D **108**, 096019 (2023).
[63] L. P. Kadanoff, W. Gotze, D. Hamblen, R. Hecht, E. A. S. Lewis, V. V. Palciauskas, M. Rayl, J. Swift, D. Aspnes, and J. Kane, Rev. Mod. Phys. **39**, 395 (1967).
[64] J. Engels and F. Karsch, Phys. Rev. D **85**, 094506 (2012).
[65] E. Grossi, A. Soloviev, D. Teaney, and F. Yan, Phys. Rev. D **104**, 034025 (2021).
[66] J. Engels and F. Karsch, Phys. Rev. D **85**, 094506 (2012).
[67] J. Engels and F. Karsch, Phys. Rev. D **90**, 014501 (2014).
[68] F. Gao and Y.-x. Liu, Phys. Rev. D **94**, 076009 (2016).
[69] G. Aarts *et al.*, Phys. Rev. D **105**, 034504 (2022).
[70] J. Braun, W.-j. Fu, J. M. Pawlowski, F. Rennecke, D. Rosenblüh, and S. Yin, Phys. Rev. D **102**, 056010 (2020).
[71] A. Holl, P. Maris, and C. D. Roberts, Phys. Rev. C **59**, 1751 (1999).